Liquid Imbibition in Ceramic-Coated Carbon Nanotube Films

Hangbo Zhao,[†] Christine Jacob,[†] Howard A. Stone,[‡] and A. John Hart*,[†] [iD]

[†]Department of Mechanical Engineering and Laboratory for Manufacturing and Productivity, Massachusetts Institute of Technology, 77 Massachusetts Avenue, Cambridge, Massachusetts 02139, United States

[‡]Department of Mechanical and Aerospace Engineering, Princeton University, Princeton, New Jersey 08544, United States

S *Supporting Information*

ABSTRACT: Understanding of the liquid imbibition dynamics in nanoporous materials is important to advances in chemical separations, phase change heat transfer, electrochemical energy storage, and diagnostic assays. We study the liquid imbibition behavior in films of ceramic-coated vertically aligned carbon nanotubes (CNTs). The nanoscale porosity of the films is tuned by conformal ceramic coating via atomic layer deposition (ALD), enabling stable liquid imbibition and precise measurement of the imbibition dynamics without capillary densification of the CNTs. We show that the imbibition rate decreases as the ceramic coating thickness increases, which effectively changes the CNT-CNT spacing and therefore decreases the permeability. We derive a model, based on Darcy's law, that incorporates an expression for the permeability of nanoscale post arrays, and we show that the model fits the experimental results with high accuracy. The tailorable porosity, along with controllable surface wettability and mechanical stability of coated CNTs, suggest their suitability for application-guided engineering, and for further investigation of imbibition behavior at finer length scales.
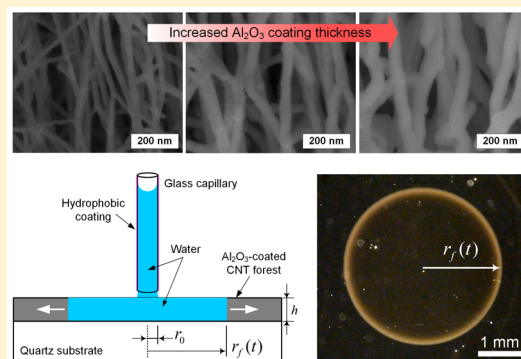
1. INTRODUCTION

Imbibition is the replacement of one fluid by an immiscible and more viscous fluid in a porous medium, and often happens as a result of the capillary suction pressure. Liquid imbibition occurs in a variety of natural and synthetic processes such as water uptake by plants,[1,2] ink writing on paper,[3] dyeing of textiles,[4,5] and lateral flow separation of biomolecules.[6] Fundamental understanding of the imbibition of nanoporous materials is also important to advanced technologies, including electrochemical storage devices, diagnostic assays, and composite materials, because nanoporous materials have a very large liquid–solid contact area, and enable tailoring of interfacial transport via their pore size and chemistry. However, while liquid imbibition in macroporous materials or microtextured surfaces is well-understood by both experimental and analytical approaches,[7−12] there has been relatively little exploration of the imbibition of bulk nanoporous materials.[13−15] Further exploration of the imbibition dynamics within nanoporous materials also requires scalable fabrication techniques that control the critical dimensions and surface properties that govern imbibition.

In particular, synthesis and assembly of carbon nanotubes (CNTs) provides a scalable route to create nanoporous materials in configurations such as random CNT networks, aligned CNT films and "forests", and long CNT fibers. Combined with the attractive thermal, mechanical, and electrical properties of CNTs, fundamental understanding of how CNT materials interact with liquids is critical to their viability as surfaces for phase change heat transfer,[16,17] battery and capacitor electrodes,[18,19] and lab-on-a-chip devices.[20] Previously, Zhou et al. studied liquid imbibition in CNT forests using fluorescent dyes;[21] however, capillary-induced aggregation of the CNTs and the dye-induced Marangoni effect complicated the flow and prevented quantitative analysis of the dynamics.

Here, we use ceramic-coated CNT forests as a means to study the capillary-driven liquid imbibition behavior in nanoporous media. Deposition of a conformal Al_2O_3 coating by atomic layer deposition (ALD) prevents capillary-induced deformation of the CNT forests, and enables quantitative study of how the permeability and imbibition rate decrease as the coating thickness is increased. A model based on Darcy's law is derived, and is found to accurately relate the effective pore size, the surface wettability, and the viscosity of the liquid to the measured imbibition dynamics.

2. METHODS

Fabrication of CNT Forests. Vertically aligned CNTs ("forests") are synthesized on quartz substrates by chemical vapor deposition (CVD). First, a supported catalyst layer of Fe/Al_2O_3 (1 nm/10 nm) is deposited on 150 mm diameter, 0.5 mm thick quartz wafers (Silicon Quest International) by electron beam evaporation (VES-2550, Temescal). The wafer is then cut into 18 mm × 18 mm pieces and placed in a CVD furnace for CNT growth. The growth recipe starts by
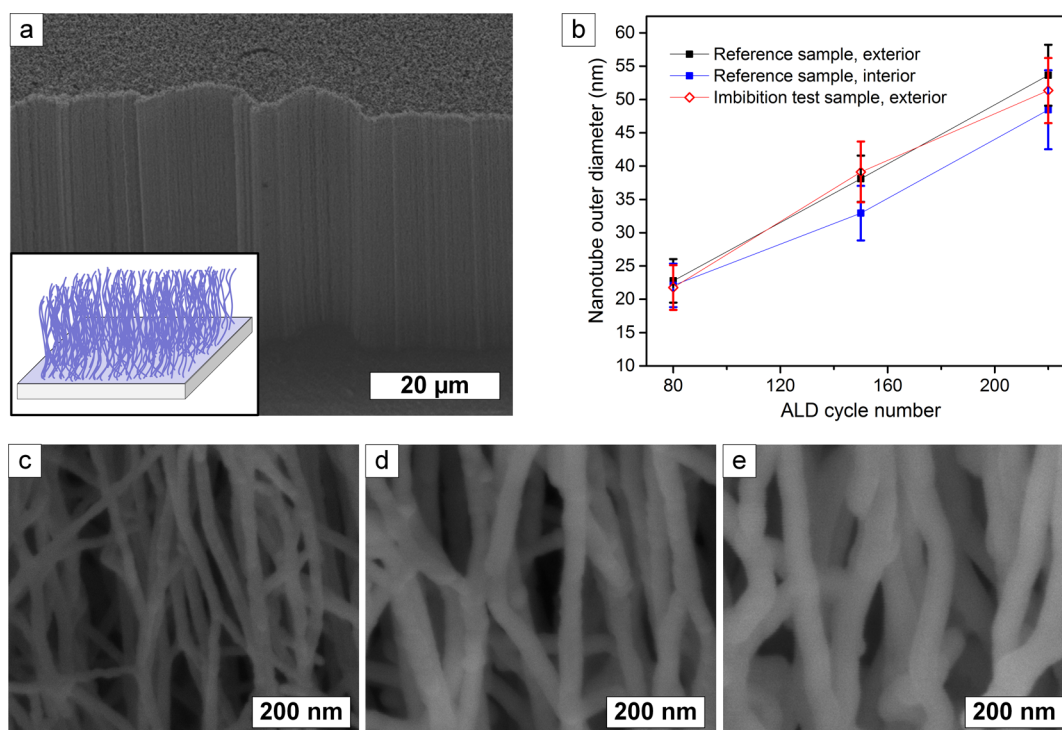
Figure 1. Control of Al_2O_3 coating thickness on CNT forests. (a) Side-view SEM image and schematic (inset) of an Al_2O_3-coated CNT forest. (b) Outer diameters of Al_2O_3-coated CNTs measured from both the exterior and interior of a coating reference sample (53 μm tall) and from the exterior of an imbibition test sample (57 μm tall) as a function of the ALD cycle number. (c−e) Side-view SEM images of CNT forests conformally coated with 80, 150, and 220 ALD cycles of Al_2O_3 coating, respectively.

flowing 100/400 sccm (standard cubic centimeters per minute) of He/H_2 while heating the furnace to 780 °C over 10 min then maintaining the furnace at 780 °C for 10 min with the same gas flow. Then, the gas flow is changed to 100/400/100 sccm of C_2H_4/He/H_2 at 780 °C for CNT growth. The vertical growth rate of the CNTs is approximately 60 μm/min and the growth duration is chosen according to the desired height. After the growth step, the furnace lid is opened, causing the tube and sample to cool rapidly while maintaining the same gas flow. When the temperature is below 100 °C, the furnace is purged with 1000 sccm of He for 5 min. After removal from the CVD system, the CNT samples are exposed to an oxygen plasma for 1 min at 30 W (AutoGlow, Glow Research). The CNT forest height is measured by optical microscopy (Zeiss Axio Imager Z1m) in the dark field mode. The height is measured at five different locations on each forest.

Atomic Layer Deposition (ALD) of Al_2O_3. Al_2O_3 is deposited onto the CNTs by atomic layer deposition (ALD; Gemstar, Arradiance Corporation). Trimethylaluminum (TMA) and ozone (O_3) are used as the metalorganic and oxidizing precursors, respectively. Using nitrogen as the carrier gas at a flow rate of 40 sccm, TMA and O_3 are sequentially pulsed into the deposition chamber (2−3 Torr, 175 °C) for 22 and 100 ms, respectively. Following each precursor pulse, the chamber is purged with 90 sccm nitrogen for 28 s.

ALD Coating Thickness Measurement. The outer diameters of the Al_2O_3-coated CNTs are measured from cross-section images taken using a Zeiss Merlin scanning electron microscope (SEM). For each CNT diameter measurement, at least 15 CNTs are measured from each of the top, middle and bottom sections of a forest. The average value of the ensemble of at least 45 measurements is used to represent the coated CNT diameter within the entire forest. The measured outer diameter is assumed to be equal to the sum of the CNT diameter and twice the Al_2O_3 coating thickness.

Imbibition Measurements. The Al_2O_3-coated CNT sample is placed on a glass slide clamped onto a manual XYZ translation stage (PT3, Thorlabs). A glass capillary (1B100-3, World Precision Instruments) with OD = 1.0 mm and ID = 0.58 mm is connected to a stainless steel holder that holds a glass capillary perpendicular to

the sample. Side view imaging is performed with a setup comprising a 2× objective (Mitutoyo) connected to a 16× zoom tube lens (NT-56-219, Edmund Optics) and a high-speed camera (Phantom Miro M310, Vision Research). For the bottom view, a DSLR camera (Nikon D5100) connected to a 5× objective (Mitutoyo) is used. A light source (model 1-150, CUDA) is placed next to the sample to provide lighting for imaging both the side and bottom views. The entire setup is placed on a vibration isolation table (ScienceDesk, Thorlabs). When performing the imbibition experiment, the glass capillary, which is filled with deionized water by capillary action, is brought into contact with the CNT surface and held in place once a liquid bridge is formed. The diameter of the spreading liquid film is measured from the bottom view video (29.97 frames per second) using ImageJ software. A stage graticule slide (GT Vision) is used as the measurement reference; one pixel in the image is measured to correspond to 5.3 μm.

Fluorosilane Coating of Glass Capillaries. It is important to not wet the outside of the capillary. Thus, to coat the capillary outer surface, the ends are first sealed neatly using kapton tape. The capillary is exposed to a fluorosilane precursor ((tridecafluoro-1,1,2,2-tetrahydrooctyl)trichlorosilane, Sigma-Aldrich) by placement next to 10 μL (~3 drops) of fluorosilane inside a vacuum desiccator for 4 h. The tape prevents deposition on the ends and inside of the capillary, allowing these surfaces to remain hydrophilic.

Contact Angle Measurement. The static contact angle is measured using a goniometer (model 590, ramé-hart) by depositing a 4 μL deionized water droplet onto the surface to be measured. For each surface, the measurement is repeated at three locations.

3. RESULTS AND DISCUSSION

To study liquid imbibition in ceramic-coated CNT forests, we prepared Al_2O_3-coated vertically aligned CNT samples with different Al_2O_3 coating thicknesses as shown in Figure 1. We first synthesized CNT forests, and then exposed the CNTs to oxygen plasma. The exposure to oxygen plasma removes the micrometer-thick dense entangled "crust" layer at the top of the

CNT forests, which represents the initial stage of growth wherein the CNTs become vertically aligned. Additionally, the removal of the crust allows for improved penetration of the ALD precursors into the forest and improves the uniformity of the CNT forest texture for the imbibition experiments.

For imbibition experiments, we employ the setup shown in Figure 2, which allows a liquid-filled glass needle to be brought
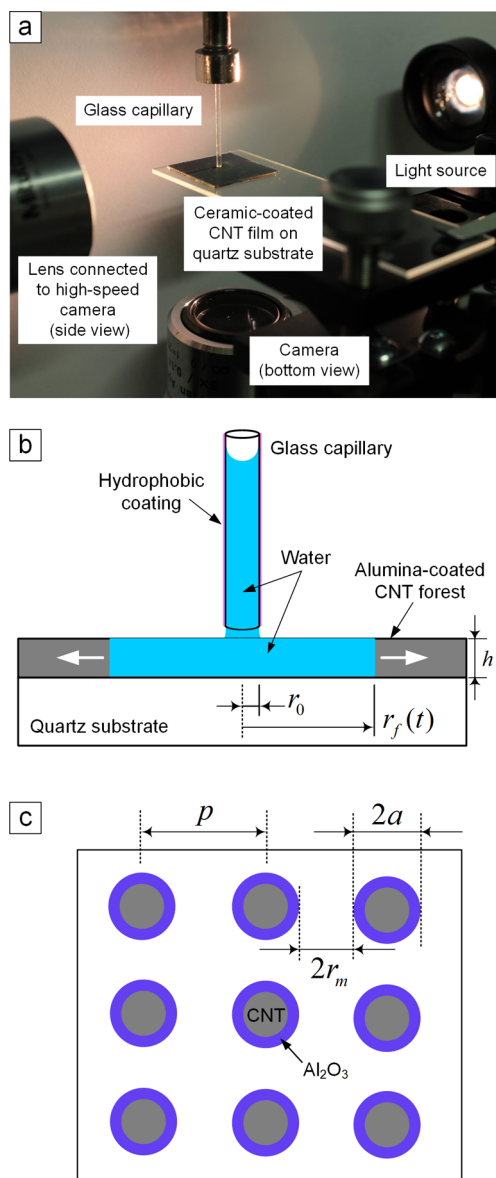

Figure 2. (a) Photograph of the experimental setup for liquid imbibition tests on Al_2O_3-coated CNT films on quartz substrates. (b) Schematic of the liquid imbibition process with initial liquid film radius r_0, time-dependent liquid front radius $r_f(t)$ and CNT forest height h. (c) Model representation (top-down view) of Al_2O_3-coated CNT forest as a square array of posts with radius a and spacing $2r_m$. The pitch $p = 2(a + r_m)$.

into contact with the substrate, along with optical imaging from the side and bottom (looking through the quartz). To prevent the liquid (deionized water) from rising up the outside surface of the capillary as liquid spreads outward into the Al_2O_3-CNT forest, the capillary is coated with a fluorosilane (see Methods). To initiate imbibition, the capillary is brought close to the top of the Al_2O_3-CNT forest; when a liquid bridge forms between

the capillary and the top of the forest surface, the forest begins to draw liquid from the capillary (Video S1). Subsequently, a growing, circular liquid front is observed as liquid is imbibed by the forest. The high-speed camera (side view) and color DSLR camera (bottom view) capture the liquid bridge formation process and the radial spreading behavior, respectively.

Liquid imbibition testing is also performed on bare CNT forests to compare wetting behavior to that of coated forests. When the above procedure is applied to a bare CNT forest, it fractures and shrinks locally as the meniscus advances (Video S2 and Figure S1a). Capillary forces exerted by the meniscus exceed the lateral strength of the CNT forest, and cause the forest to densify.[22,23] Therefore, coating of the CNTs by a thin layer that reinforces the CNT forest is critical to enable controlled imbibition measurements wherein CNT densification does not occur. The CNTs are coated with Al_2O_3 using atomic layer deposition (ALD) with trimethylaluminum (TMA) and ozone (O_3) being the precursors. Ozone provides the twofold benefit of etching the surface of the CNTs as well as reducing TMA to form Al_2O_3. Etching CNTs increases the density of surface defects, which serve as nucleation sites for the coating.[24] This coating is conformal, and the growth rate is approximately 0.1 nm per deposition cycle. The ALD Al_2O_3 layer is slightly hydrophilic with a measured water contact angle of $\theta = 83.2 \pm 0.2°$ (Figure S4) on a flat Al_2O_3 surface. Notably, the water contact angle on pristine Al_2O_3 is small ($\sim 10°$);[25] however, the hydrophilicity of the deposited Al_2O_3 layer decreases due to hydrocarbon adsorption from the ambient air.[26]

Upon water imbibition of CNT forest samples coated by 40 cycles of alumina ALD, we do not observe significant elastocapillary densification, yet small cracks are still formed (Figure S1b). On samples with 80 cycles of ALD Al_2O_3 (~ 8 nm thick coating), no densification or cracking is observed after imbibition (Figure S1c). Previously, Tawfick et al. found that the CNT densification is suppressed by an ALD coating because it increases the effective bending rigidity of the coated CNTs and adheres the CNTs at contact points, thus significantly increasing the in-plane and shear moduli of the forest.[27] Therefore, to allow for measurement of liquid imbibition in stable, rigid nanoporous CNT forests, we applied a minimum of 80 cycles of ALD coating.

To study the dynamics of imbibition a series of samples with different CNT heights is prepared and taken through the same sequence of ALD coating, imbibition measurement, and further coating (Figure S2). As such, imbibition tests are performed on each sample after exposure to 80, 150, and 220 total ALD cycles. This incremental coating procedure ensures that the CNT diameter measurements and liquid imbibition tests are performed with increasing Al_2O_3 coating thicknesses on the same sample, which therefore preserves the initial CNT forest morphology, and decouples the influences of CNT morphology and coating thickness on the liquid imbibition behavior.

On each sample, the coating thickness is determined by averaging measurements from high resolution SEM images along the exterior and interior of the forest (at least 45 measurements per sample; see Methods). In Figure 1b, we show the relationship between ALD cycle number and the resulting coating thickness. Due to diffusion limitation of the ALD precursors, it is expected that the coating thickness on the interior and base of the CNT forest would be less than at the top and outer surfaces.[28] The differences in the diameters measured from exterior and interior of a reference sample (53
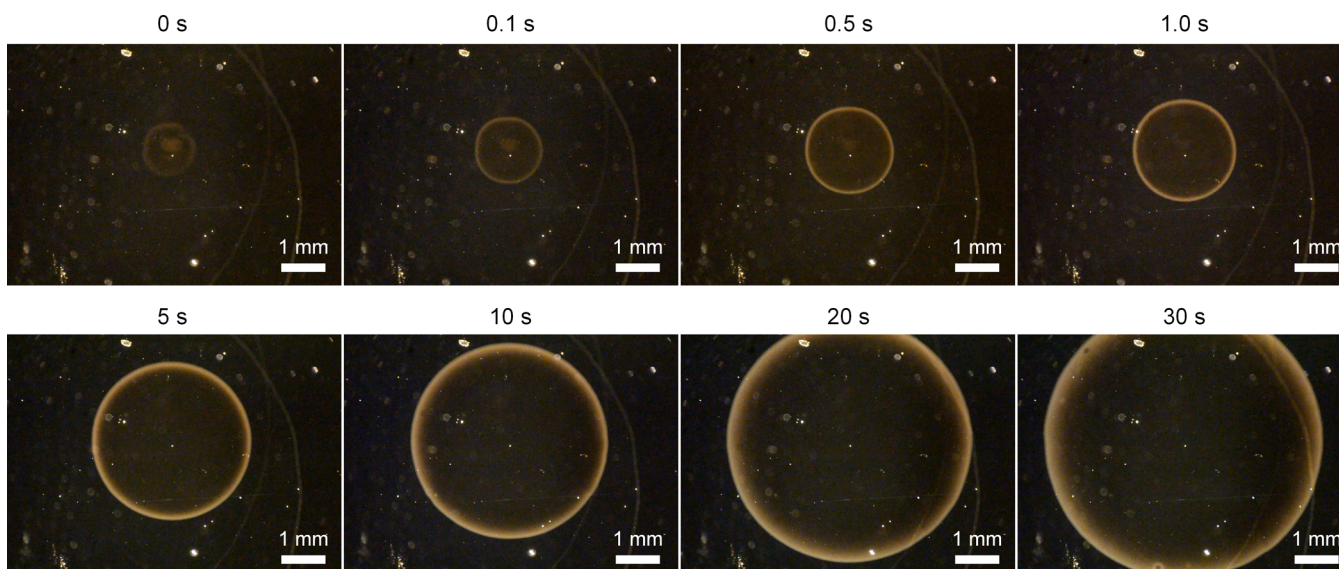
Figure 3. Snapshots from the bottom-view camera of deionized water imbibition in Al$_2$O$_3$-CNT forest (150 ALD cycles) at t = 0, 0.1, 0.5, 1, 5, 10, 20, and 30 s.

μm height, see Table S1 in the Supporting Information) are used to estimate the average Al$_2$O$_3$-CNT diameters in the interior of the forest sample used for liquid imbibition tests. The same exterior−interior diameter difference after each coating step is used to estimate the interior Al$_2$O$_3$-CNT diameters of the imbibition test sample (see Table S2 in the Supporting Information).

The dynamics of liquid imbibition in the Al$_2$O$_3$-coated CNT forest are now examined by measurement of the radial imbibition distance $r_f(t)$ versus time, which is captured using the bottom-view imaging path. As described above, a series of imbibition tests is performed on each sample, at increased Al$_2$O$_3$ coating thicknesses; at each thickness, the imbibition test is repeated three times. Frames of a bottom-view video (Video S3) of a representative imbibition test are presented in Figure 3. The lighting provides a clear contrast between the wetted and dry areas as water spreads within the forest, showing a clear circular imbibition front that grows with time. The starting point (t = 0 s) is assigned based on the frame in the bottom-view video where the liquid film is first visible. The initial wetted area is defined at the instant when the liquid bridge is formed, as observed in the side-view high-speed imaging taken simultaneously, which matches the bottom-view measurement within 2% error.

The dynamics of imbibition are modeled according to the schematic diagram in Figure 2b. The liquid wets the Al$_2$O$_3$-coated CNT surface with an initial radius r_0, and then spreads radially with a time-dependent radius $r_f(t)$ at the liquid front. The properties of the deionized water are assumed to be (at 25 °C), density $\rho = 0.997 \times 10^3$ kg/m^3, dynamic viscosity $\mu = 8.94 \times 10^{-4}$ Pa·s and surface tension $\gamma = 72 \times 10^{-3}$ N/m. Typical Al$_2$O$_3$-coated CNT dimensions are radius ∼ 10 nm, spacing ∼ 100 nm, and height ∼ 50 μm. With the characteristic length L_c being the CNT-CNT spacing (∼100 nm) and measured characteristic velocity ∼1 mm/s, the Reynolds number is approximately Re = $\frac{\rho U L_c}{\mu} \approx 10^{-4} \ll 1$. Therefore, the inertial-dominated initial stage of wetting is negligible compared to the measured time frame (30 s), and the flow can be treated as a quasi-steady-state Stokes flow, driven by the capillary force and

balanced by the resisting viscous drag through the nanoporous forest. Liquid evaporation and the flow resistance from the glass capillary are negligible (see the Supporting Information).

To model the radial imbibition of liquid, Darcy's law is applied in cylindrical coordinates,

$$\frac{Q}{A} = -\frac{k}{\mu}\frac{\partial P}{\partial r} \tag{1}$$

where Q is the volumetric flow rate, A is the liquid cross-sectional area ($A = 2\pi rh$), and k is the permeability of the Al$_2$O$_3$-coated CNT forest. The volumetric flow rate can be written as

$$Q = 2\pi rh\frac{dr_f}{dt}\phi \tag{2}$$

where ϕ is the porosity of the forest and $r_f(t)$ is the position of the liquid front. Substituting eq 2 into eq 1 and integrating from the liquid source ($r = r_0$) to the liquid front ($r = r_f(t)$) yields

$$P_c = \frac{\mu\phi}{k}r_f\frac{dr_f}{dt}\ln\frac{r_f}{r_0} \tag{3}$$

where P_c is the capillary pressure which is expressed as

$$P_c = \frac{2\gamma\cos\theta}{r_m} \tag{4}$$

Here, r_m is the mean pore radius of the forest and θ is the contact angle of water on a flat Al$_2$O$_3$-coated silicon wafer (measured $\theta = 83.2 \pm 0.2°$). Equating eqs 3 and 4 and introducing a nondimensional parameter, $R_f \equiv \frac{r_f}{r_0}$, yields

$$\frac{R_f^2\left(\ln R_f - \frac{1}{2}\right) + \frac{1}{2}}{\frac{t}{r_0^2}} = \frac{4k\gamma\cos\theta}{\mu\phi r_m} \equiv C \tag{5}$$

The right side of eq 5 depends on the properties of the liquid and nanoporous film, which are constant in each test; the constant C in eq 5 is introduced for convenience.

The CNTs within the forest have pronounced waviness upon their general vertical alignment, and as a result are found in both isolated and bundled positions with a distribution of spacings.[29] In spite of this feature, we investigated the utility of approximating the forest as a square array of vertical posts when modeling the imbibition dynamics. In this array, the posts have radius a, pitch (center-to-center distance) p, and height h (Figure 2c). Because of the extremely high aspect ratio of the CNTs ($\frac{h}{a} > 10^3$), the capillary pressure is independent of the height h, and the mean pore radius in eq 4 can be approximated as $r_m = \frac{p}{2} - a$. Several solutions for Stokes flow through a square array of posts have been shown to accurately predict the permeability for a wide range of materials with solid volume fractions smaller than 0.3,[30] among which Sangani and Acrivos derived an analytical expression for the permeability[31]

$$k = \frac{a^2}{8\varepsilon}(-\ln \varepsilon - 1.476 + 2\varepsilon - 1.774\varepsilon^2 + 4.076\varepsilon^3 + O(\varepsilon^4)) \tag{6}$$

where the solid volume fraction in a square array is $\varepsilon = \frac{\pi a^2}{p^2}$. Neglecting the higher-order terms in eq 6, the right side of eq 5 can be written as

$$C = \frac{\gamma \cos \theta}{\pi \mu} \frac{p^4}{(p^2 - \pi a^2)(p - 2a)} \left(-2\ln \frac{a}{p} - \ln \pi \right.$$
$$\left. - 1.476 + \frac{2\pi a^2}{p^2} - \frac{1.774\pi^2 a^4}{p^4} + \frac{4.076\pi^3 a^6}{p^6}\right) \tag{7}$$

For our nanoporous materials, the Al_2O_3-CNT radius a is measured and estimated from side-view SEM imaging after each coating step, yet the pitch p cannot be directly measured due to the waviness and polydispersity of CNTs in the forest. Hence we choose p as the only fitting parameter in the model. When additional coating is applied to each sample, we first assume that p remains constant and the nanotube radius a increases, resulting in a decrease in the pore radius r_m.

Plotting of the experimental imbibition data, according to the nondimensional representation of the imbibition distance $R_f^2\left(\ln R_f - \frac{1}{2}\right) + \frac{1}{2}$ versus $\frac{t}{r_0^2}$ shows straight line trends (Figure 4a), as predicted by eq 5. The slopes of the trend lines decrease with increasing Al_2O_3 coating thicknesses, and the linear correlations are strong (coefficients $r^2 > 0.997$) in all tests. The data at $R_f < 3$ is excluded due to the possibility of unsteady flow in the early stage of imbibition. Uncertainties introduced by the measurements of the initial wetted radius r_0 and the liquid front radius r_f are calculated (see the Supporting Information); these total uncertainties increase with the liquid spreading distance. The maximum uncertainties of the three repeated experiments after each coating step are shown as error bars in Figure 4a.

Also, in Figure 4a, we compare the model (eqs 5 and 7) to the experimental results. For each sample, linear fitting of the experimental data with 80 ALD cycles of Al_2O_3 coating is first performed and the average fitted slope of the three tests is calculated. Then the parameter p in the model is calculated by fitting the model to the average measured slope. For a 57 μm tall CNT forest shown in Figure 4a, the CNT pitch is calculated to be $p = 78$ nm. For subsequent coatings, the same calculated
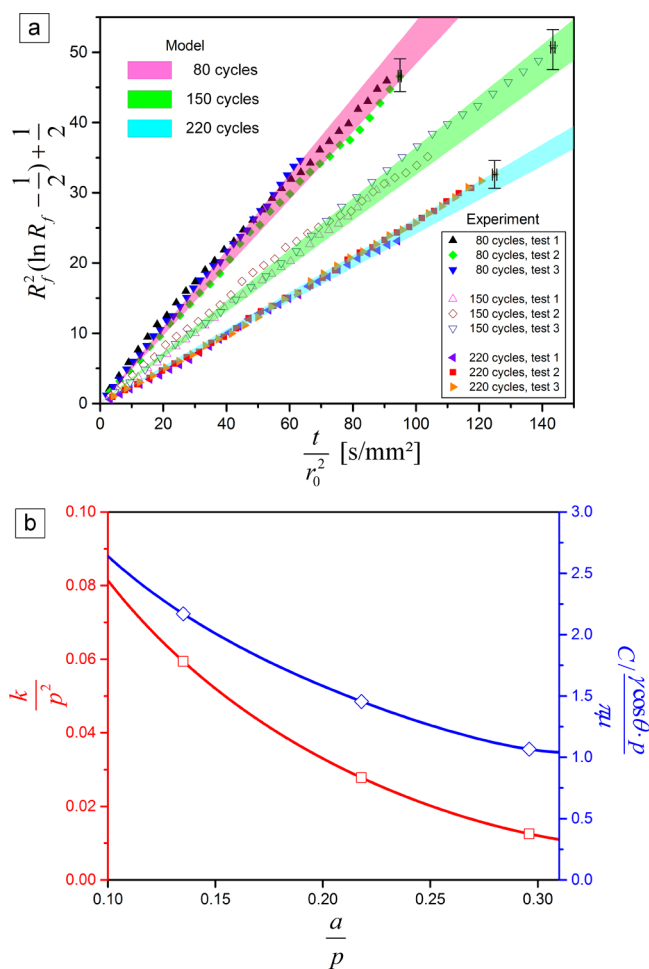

Figure 4. (a) Comparison of model and experiments of liquid imbibition on a 57 μm tall Al_2O_3-CNT forest, with fitted pitch value p = 78 nm. (b) Nondimensional permeability k/p and slope $C/(\gamma \cos \theta p/\pi \mu)$ determined by the model versus the ratio of coated CNT radius to pitch (a/p). The data points indicate the a/p values achieved in experiments.

p is used while the radius a increases, based on which the nondimensional imbibition rates from the model are calculated according to eq 5 and 7. The uncertainties in the model introduced by the measurements of the contact angle θ and the Al_2O_3-coated CNT radius a for each coating thickness are calculated (see the Supporting Information) and shown as narrow shaded bands in Figure 4a. Within the uncertainty range, the model accurately predicts the position of the liquid front versus time for all coating thicknesses. We also performed calculations and fitting for a hexagonal post array geometry.[31] Like the square array approximation, this approach also captures the experimental data well (see the Supporting Information), suggesting that the definition of an effective average spacing is sufficient to understand the imbibition dynamics at these dimensional scales, in spite of the polydisperse spacing among the CNTs in the forest.

We also investigated the influence of CNT forest height on the imbibition dynamics. In addition to the sample (57 μm height) shown above in Figure 4a, CNT samples with heights of 48 and 20 μm were also prepared and tested using the same procedure. The measured and estimated Al_2O_3-CNT diameter values are listed in Table S2, using the exterior-interior coating thickness difference from the reference sample (Figure 1b).

The experimental data and corresponding model curves are plotted in Figure S5; all samples show highly linear imbibition behavior. Within the uncertainty range, the model closely matches the data for the taller (48 μm) forest, with a fitting pitch p = 77 nm. Greater deviation between the model and data is observed for the shorter (20 μm height) forest. The deviation is likely caused by height-dependent variation of CNT density and alignment, which is well-known in CNT forest growth;[29] this changes the local pore size which is further determined by the local kinetics of ALD coating. Therefore, our estimation of the average Al_2O_3-coated CNT diameter and effective pore size is less accurate for the short forest sample.

In Figure 4b, we show how the permeability k and slope C depend on the coating thickness; these are presented in nondimensional forms using the fixed pitch p for each sample. With increasing coating thickness, the nanotube radius/pitch ratio (a/p) increases, leading to monotonically decreasing permeability and slope (i.e., liquid spreading rate). Note that as the spacing of the coated CNTs decreases, the viscous drag increases (as a result of lower permeability) faster than the capillary driving force, causing the liquid imbibition rate to decrease. For the sample studied in Figure 4a, the a/p values corresponding to the diameter values of the Al_2O_3-coated CNTs are represented by the markers on Figure 4b. The corresponding maximum solid volume fraction is ε = 0.29 (a/p = 0.296 for 220 cyeles of ALD coating). Within this range the permeability model adopted from Sangani and Acrivos (eq 6) is shown to match experimental data from various sources well.[30]

However, the permeability model in eq 6 does not apply to highly dense post arrays. For post arrays with a/p greater than approximately 0.3, the permeability and imbibition rate are expected to decrease monotonically with increasing thickness as a/p reaches the theoretically maximum value of 0.5 at which the spacing is zero (see Figure S6 and Supporting Information text). However, the same scaling does not apply as the pore size is reduced to a few nanometers or subnanometers, as the no-slip boundary condition may no longer hold and the interfacial viscous forces in nanoconfined fluids such as water can increase dramatically as the gap becomes smaller than ca. 1−2 nm.[32,33] Imbibition in this smaller pore size regime is interesting and important, but is beyond scope of the current work.

4. CONCLUSIONS

We have shown that the dynamics of liquid imbibition can be precisely tuned by controlling the nanoscale porosity of ceramic-coated CNT forests. Our analytical and experimental understanding of imbibition dynamics in coated CNT forests is important for applications that can utilize nanoporous materials including fluidic devices, phase change heat transfer surfaces, and liquid-based sensors. For instance, the imbibition rate is directly related to the wickability of the porous surfaces, which has been found to influence the boiling critical heat flux.[34] In addition, conformal coating of the CNTs can effectively tune the pore size from ∼100 nm to a few nanometers, or even completely close the CNT-CNT gap. This precise and large range of tunability of pore size may also be attractive for size-based biomolecular separation, because this pore size range is comparable to the length scales of DNAs and proteins.[35] CNTs can be coated conformally by metals, ceramics and polymers,[36−38] suggesting that CNT-based imbibition materials can be designed for various operating conditions while preserving liquid-stable nanoporosity. Moreover, the mechanical robustness, the high electrical conductivity of CNTs, and

the capability of forming CNTs into three-dimensional (3D) microarchitectures,[39,40] make this approach promising for the design of liquid-stable nanoporous microstructures with complex 3D geometries.

■ ASSOCIATED CONTENT

ⓢ Supporting Information

The Supporting Information is available free of charge on the ACS Publications website at DOI: 10.1021/acs.langmuir.6b03661.

> Measurement of the Al_2O_3-coated CNT diameters; neglecting liquid evaporation and flow resistance in the glass capillary; uncertainty of model and experimental data; comparison of model results for square vs hexagonal CNT packing geometries; dependence of permeability k and model slope C on a/p; SEM images (PDF)
> Video showing formation of liquid bridge between the capillary and the CNT forest surface (AVI)
> Video showing bare CNT forest shrinking upon liquid imbibition (AVI)
> Video showing liquid imbibition in Al_2O_3-coated CNT film (AVI)

■ AUTHOR INFORMATION

Corresponding Author

*E-mail: ajhart@mit.edu.

ORCID ⓘ

A. John Hart: 0000-0002-7372-3512

Notes

The authors declare no competing financial interest.

■ ACKNOWLEDGMENTS

■ REFERENCES

(1) Pickard, W. F. The ascent of sap in plants. *Prog. Biophys. Mol. Biol.* **1981**, 37, 181−229.

(2) Wheeler, T. D.; Stroock, A. D. The transpiration of water at negative pressures in a synthetic tree. *Nature* **2008**, 455, 208−212.

(3) Kim, J.; Moon, M.-W.; Lee, K.-R.; Mahadevan, L.; Kim, H.-Y. Hydrodynamics of writing with ink. *Phys. Rev. Lett.* **2011**, 107, 264501.

(4) Pezron, I.; Bourgain, G.; Quéré, D. Imbibition of a fabric. *J. Colloid Interface Sci.* **1995**, 173, 319−327.

(5) Perwuelz, A.; Mondon, P.; Caze, C. Experimental study of capillary flow in yarns. *Text. Res. J.* **2000**, 70, 333−339.

(6) Posthuma-Trumpie, G. A.; Korf, J.; van Amerongen, A. Lateral flow (immuno) assay: its strengths, weaknesses, opportunities and threats. A literature survey. *Anal. Bioanal. Chem.* **2009**, *393*, 569−582.

(7) Dullien, F. A. *Porous Media: Fluid Transport and Pore Structure*; Academic Press: New York, 1979.

(8) Ishino, C.; Reyssat, M.; Reyssat, E.; Okumura, K.; Quéré, D. Wicking within forests of micropillars. *EPL* **2007**, *79*, 56005.

(9) Courbin, L.; Denieul, E.; Dressaire, E.; Roper, M.; Ajdari, A.; Stone, H. A. Imbibition by polygonal spreading on microdecorated surfaces. *Nat. Mater.* **2007**, *6*, 661−664.

(10) Courbin, L.; Bird, J. C.; Reyssat, M.; Stone, H. A. Dynamics of wetting: from inertial spreading to viscous imbibition. *J. Phys.: Condens. Matter* **2009**, *21*, 464127.

(11) Mendez, S.; Fenton, E. M.; Gallegos, G. R.; Petsev, D. N.; Sibbett, S. S.; Stone, H. A.; Zhang, Y.; Lopez, G. P. Imbibition in porous membranes of complex shape: quasi-stationary flow in thin rectangular segments. *Langmuir* **2010**, *26*, 1380−1385.

(12) Xiao, R.; Enright, R.; Wang, E. N. Prediction and optimization of liquid propagation in micropillar arrays. *Langmuir* **2010**, *26*, 15070−15075.

(13) Gruener, S.; Hofmann, T.; Wallacher, D.; Kityk, A. V.; Huber, P. Capillary rise of water in hydrophilic nanopores. *Phys. Rev. E* **2009**, *79*, 067301.

(14) Grzelakowski, C.; Ben Jazia, D.; Lebeau, B.; Vonna, L.; Dupuis, D.; Haidara, H. On the influence of pore structure on the free-imbibition of sessile drops into nanoporous substrates. *Langmuir* **2009**, *25*, 5855−5860.

(15) Xue, Y.; Markmann, J.; Duan, H.; Weissmüller, J.; Huber, P. Switchable imbibition in nanoporous gold. *Nat. Commun.* **2014**, *5*, 4237.

(16) Cai, Q.; Chen, C.-L. Design and test of carbon nanotube biwick structure for high-heat-flux phase change heat transfer. *J. Heat Transfer* **2010**, *132*, 052403.

(17) Ahn, H. S.; Sinha, N.; Zhang, M.; Banerjee, D.; Fang, S.; Baughman, R. H. Pool boiling experiments on multiwalled carbon nanotube (MWCNT) forests. *J. Heat Transfer* **2006**, *128*, 1335−1342.

(18) Lu, W.; Qu, L.; Henry, K.; Dai, L. High performance electrochemical capacitors from aligned carbon nanotube electrodes and ionic liquid electrolytes. *J. Power Sources* **2009**, *189*, 1270−1277.

(19) Welna, D. T.; Qu, L.; Taylor, B. E.; Dai, L.; Durstock, M. F. Vertically aligned carbon nanotube electrodes for lithium-ion batteries. *J. Power Sources* **2011**, *196*, 1455−1460.

(20) Fachin, F.; Wardle, B. L.; Chen, G. D.; Toner, M. Integration of vertically-aligned carbon nanotube forests in microfluidic devices for multiscale isolation of bioparticles. *IEEE Sensors* **2010**, 47−51.

(21) Zhou, J. J.; Noca, F.; Gharib, M. Flow conveying and diagnosis with carbon nanotube arrays. *Nanotechnology* **2006**, *17*, 4845−4853.

(22) Zhao, Z.; Tawfick, S. H.; Park, S. J.; De Volder, M.; Hart, A. J.; Lu, W. Bending of nanoscale filament assemblies by elastocapillary densification. *Phys. Rev. E* **2010**, *82*, 041605.

(23) Cui, K.; Chiba, T.; Omiya, S.; Thurakitseree, T.; Zhao, P.; Fujii, S.; Kataura, H.; Einarsson, E.; Chiashi, S.; Maruyama, S. Self-assembled microhoneycomb network of single-walled carbon nanotubes for solar cells. *J. Phys. Chem. Lett.* **2013**, *4*, 2571−2576.

(24) Lushington, A.; Liu, J.; Tang, Y.; Li, R.; Sun, X. Surface modification of nitrogen-doped carbon nanotubes by ozone via atomic layer deposition. *J. Vac. Sci. Technol., A* **2014**, *32*, 01A124.

(25) Azimi, G.; Dhiman, R.; Kwon, H.-M.; Paxson, A. T.; Varanasi, K. K. Hydrophobicity of rare-earth oxide ceramics. *Nat. Mater.* **2013**, *12*, 315−320.

(26) Karaman, M. E.; Antelmi, D. A.; Pashley, R. M. The production of stable hydrophobic surfaces by the adsorption of hydrocarbon and fluorocarbon carboxylic acids onto alumina substrates. *Colloids Surf., A* **2001**, *182*, 285−298.

(27) Tawfick, S.; Zhao, Z.; Maschmann, M.; Brieland-Shoultz, A.; De Volder, M.; Baur, J. W.; Lu, W.; Hart, A. J. Mechanics of capillary forming of aligned carbon nanotube assemblies. *Langmuir* **2013**, *29*, 5190−5198.

(28) Yazdani, N.; Chawla, V.; Edwards, E.; Wood, V.; Park, H. G.; Utke, I. Modeling and optimization of atomic layer deposition processes on vertically aligned carbon nanotubes. *Beilstein J. Nanotechnol.* **2014**, *5*, 234−244.

(29) Bedewy, M.; Meshot, E. R.; Reinker, M. J.; Hart, A. J. Population growth dynamics of carbon nanotubes. *ACS Nano* **2011**, *5*, 8974−8989.

(30) Jackson, G. W.; James, D. F. The permeability of fibrous porous media. *Can. J. Chem. Eng.* **1986**, *64*, 364−374.

(31) Sangani, A. S.; Acrivos, A. Slow flow past periodic arrays of cylinders with application to heat-transfer. *Int. J. Multiphase Flow* **1982**, *8*, 193−206.

(32) Ortiz-Young, D.; Chiu, H.-C.; Kim, S.; Voïtchovsky, K.; Riedo, E. The interplay between apparent viscosity and wettability in nanoconfined water. *Nat. Commun.* **2013**, *4*, 2482.

(33) Li, T.-D.; Gao, J.; Szoszkiewicz, R.; Landman, U.; Riedo, E. Structured and viscous water in subnanometer gaps. *Phys. Rev. B: Condens. Matter Mater. Phys.* **2007**, *75*, 115415.

(34) Rahman, M. M.; Ölçeroğlu, E.; McCarthy, M. Role of wickability on the critical heat flux of structured superhydrophilic surfaces. *Langmuir* **2014**, *30*, 11225−11234.

(35) Kelley, S. O.; Mirkin, C. A.; Walt, D. R.; Ismagilov, R. F.; Toner, M.; Sargent, E. H. Advancing the speed, sensitivity and accuracy of biomolecular detection using multi-length-scale engineering. *Nat. Nanotechnol.* **2014**, *9*, 969−980.

(36) Kim, J. W.; Kim, B.; Park, S. W.; Kim, W.; Shim, J. H. Atomic layer deposition of ruthenium on plasma-treated vertically aligned carbon nanotubes for high-performance ultracapacitors. *Nanotechnology* **2014**, *25*, 435404.

(37) Li, X. L.; Li, C.; Zhang, Y.; Chu, D. P.; Milne, W. I.; Fan, H. J. Atomic layer deposition of ZnO on multi-walled carbon nanotubes and its use for synthesis of CNT-ZnO heterostructures. *Nanoscale Res. Lett.* **2010**, *5*, 1836−1840.

(38) Lachman, N.; Xu, H.; Zhou, Y.; Ghaffari, M.; Lin, M.; Bhattacharyya, D.; Ugur, A.; Gleason, K. K.; Zhang, Q. M.; Wardle, B. L. Tailoring thickness of conformal conducting polymer decorated aligned carbon nanotube electrodes for energy storage. *Adv. Mater. Interfaces* **2014**, *1*, 1400076.

(39) De Volder, M.; Park, S.; Tawfick, S.; Hart, A. J. Strain-engineered manufacturing of freeform carbon nanotube microstructures. *Nat. Commun.* **2014**, *5*, 4512.

(40) Park, S. J.; Zhao, H.; Kim, S.; De Volder, M.; Hart, A. J. Predictive synthesis of freeform carbon nanotube microarchitectures by strain-engineered chemical vapor deposition. *Small* **2016**, *12*, 4393−4403.